



# Geomagnetic Activity Following Interplanetary Shocks in Solar Cycles 23 and 24

Ezequiel Echer<sup>1</sup>  · Aline de Lucas<sup>2</sup> · Rajkumar Hajra<sup>3,6</sup> · Adriane Marques de Souza Franco<sup>4</sup> · Mauricio J. A. Bolzan<sup>5</sup> · Luis Eduardo Sales do Nascimento<sup>2</sup>

Received: 22 November 2022 / Accepted: 22 March 2023  
© The Author(s) under exclusive licence to Sociedade Brasileira de Física 2023

## Abstract

Interplanetary shocks are important precursors of interplanetary coronal mass ejections (ICMEs) and corotating interaction regions (CIRs). The shock compression and draping effects on the interplanetary magnetic field (IMF) in sheaths can lead to significant geomagnetic activity. We identified 297 fast forward shocks observed by the *Advanced Composition Explorer* spacecraft upstream of the Earth, and analyzed their geomagnetic impacts in solar cycle (SC) 23 (1998–2008) and SC24 (2009–2018). The shock (normalized) occurrence rate is found to be significantly higher during SC23 compared to SC24, and it exhibits a stronger correlation with the sunspot number during SC23 (correlation coefficient  $r = 0.93$ ) than during SC24 ( $r = 0.86$ ). The average shock compressions of the IMF magnitude and plasma density are  $\approx 2.0$  and  $\approx 2.4$ , respectively, with no significant correlation with geomagnetic activity. Variations of solar wind parameters and geomagnetic activity indices following the shock arrival are explored. An interval of 6 h (3 days) following the shock is characterized by the average peak values of solar wind speed  $V_{sw} = 525$  (610)  $\text{km s}^{-1}$ , IMF  $B_z = -6.5$  ( $-11.1$ ) nT, and electric field  $E_y = 3.5$  (6.1)  $\text{mV m}^{-1}$ , followed by the average peak geomagnetic indices of  $Dst = -36$  ( $-83$ ) nT,  $ap = 56$  (92) nT, and  $AE = 733$  (1061) nT. About 25% and 63% of the shocks are followed by geomagnetic storms with  $Dst \leq -50$  nT in the following 6-h and 3-day periods, respectively. The percentages of shocks followed by the auroral activity level  $AE > 500$  nT are  $\approx 65\%$  and  $\approx 96\%$  for the short and long intervals, respectively. For the  $ap$  activity level ( $> 56$  nT), the geoeffective shocks are  $\approx 30\%$  and  $\approx 60\%$ , respectively. The overall increase in the geomagnetic activity after the shock arrival for the longer shock-preceded interval is possibly due to inclusion of contributions from shock driver (ICME or CIR) fields. It can be concluded that an interplanetary fast forward shock has a probability of 1/4 to be followed by geomagnetic storms, and of 2/3 to be followed by significant auroral activity. We derived probability distribution functions of geomagnetic indices for the 6-h and 3-day intervals following shocks. The results might be important for space weather modeling and applications.

**Keywords** Solar wind · Shock waves · Coronal mass ejections · Magnetic reconnection · Magnetosphere · Geomagnetic disturbances · Solar cycle

✉ Ezequiel Echer  
ezequiel.echer@gmail.com

<sup>1</sup> Instituto Nacional de Pesquisas Espaciais,  
São José dos Campos, Brazil

<sup>2</sup> Instituto Federal de Educacao, Ciencia e Tecnologia de São  
Paulo, Jacarei, Brazil

<sup>3</sup> Indian Institute of Technology Indore, Indore, India

<sup>4</sup> Universidade Federal do Sul e Sudeste do Para, Maraba,  
Brazil

<sup>5</sup> Universidade Federal de Jatai, Jatai, Brazil

<sup>6</sup> CAS Key Laboratory of Geospace Environment, School  
of Earth and Space Sciences, University of Science  
and Technology of China, Hefei, China

## 1 Introduction

The solar wind [1] is a supermagnetosonic, magnetized plasma that is continuously emitted from the solar corona, and fills the interplanetary space. During transient activity in the Sun, like coronal mass ejections (CMEs), huge amount of solar plasma is sporadically ejected into space [2]. When CMEs propagate faster than the local magnetosonic wave speed ( $V_{ms}$ ), their interplanetary remnants, called interplanetary CMEs or ICMEs, can drive fast shocks. On the other hand, the interaction between a solar wind high-speed stream (HSS) emanated from a coronal hole with the background (slow) solar wind leads to a corotating interaction region (CIR) formation [3].

However, CIRs are usually not bounded by shocks near the Earth's orbit (at 1 AU from the Sun), with only a few CIRs driving fully formed shocks [4–16].

Fast interplanetary shocks are observed when the shock speed relative to the upstream solar wind flow is higher than  $V_{ms}$ . A fast shock can be classified as a forward shock (FS), when propagating away from the Sun, or as a reverse shock (RS), when propagating toward the Sun. However, both are convected outward by the faster moving solar wind flow [6, 7, 12, 17]. From the in situ spacecraft observation, an FS is characterized by sharp increases in the solar wind speed  $V_{sw}$ , proton density  $N_p$ , temperature  $T_p$ , and the interplanetary magnetic field (IMF) magnitude  $B_0$ . On the other hand, a RS is characterized by a sharp increase in  $V_{sw}$ , with simultaneous decreases in  $N_p$ ,  $T_p$  and  $B_0$ . As the solar wind evolves through the heliosphere, interplanetary shock occurrence and their characteristics change [18–20]. At 1 AU, most of the shocks are FSs driven by ICMEs [12, 13, 21–23].

A fast FS can compress the dayside magnetopause (earthward). This motion generates a fast wave propagating radially earthward and azimuthally around the Earth. Geomagnetic effects of shocks, such as sudden impulses (SI<sup>+</sup>s) and storm sudden commencements (SSCs), have been studied before the space era [24]. More recently, it has been found that shocks can produce fast acceleration of relativistic electrons in the radiation belts and inside the plasmasphere through the shock induced electric fields (e.g., [25–27]). In addition, the effect of the shock impact angle on the geoeffectiveness of shocks has also been recently studied [28]. Several other studies have been conducted on other magnetospheric effects of interplanetary shocks, such as the generation of the dayside aurora, creation of new radiation belts, triggering of substorms, and generation of intense geomagnetically induced currents (GICs) (e.g., [27, 29–31] and references therein).

The region between the interplanetary shock and its possible interplanetary driver is called the interplanetary sheath. In this region, there are geomagnetic effects due to shock compression or deflection of IMF and its draping around its driver.

In addition, when there is an intense and long-duration precursor IMF southward component ( $B_s$ ) upstream of the shock, the impacts are dramatically intensified [32]. Intense  $B_s$  may also occur in the sheath region, downstream the shock, caused by draping effects around its driver or by the compression of the preexisting  $B_s$  fields [33–35].

Besides these direct shock and sheath effects on geomagnetic activity, intervals of solar wind following shocks are usually permeated by intense and long-duration  $B_s$  in their driver ICMEs and CIRs, which leads to intense geomagnetic storm activity [36].

The aims of the present work are to compile a list of all interplanetary fast FSs and to study their geomagnetic

effects during the last two solar cycles. The shock impacts will be referred as the “shock geoeffectiveness”. Previous works [37–40] have analyzed the geomagnetic indices Dst, Kp and AE during a period of about 2 to 3 days following the shock arrival at Earth to determine the shock geoeffectiveness. It has been found that  $\approx 50$ –60% of the shocks are followed by moderate to intense magnetic storms. Shocks were found to be more often followed by enhanced auroral electrojet (AE) activity compared to the ring current (Dst) activity. In addition, the shock geoeffectiveness was reported to be lower than the ICME geoeffectiveness, and higher than the CIR geoeffectiveness, as expected [39, 40].

The solar wind plasma and magnetic field measurements by NASA's *Advanced Composition Explorer* (ACE) spacecraft are used in order to identify all FSs upstream of Earth during 1998–2018, covering most of solar cycle (SC) 23 (1998–2008) and SC24 (2009–2018). The plasma density and IMF compression ratios across the shocks are computed. In addition, we estimate the solar wind characteristic features that lead to significant geomagnetic activity in intervals following the FSs, namely the averages of the peak  $V_{sw}$ ,  $B_s$ , and the interplanetary convection electric field dawn-to-dusk component  $E_y$  as well as the geomagnetic indices ap, AE and Dst during a 6-h and a 3-day periods following the FS arrivals. Further, probability distribution functions for the peak values of the geomagnetic indices are derived fitting the histograms of observations for the 6-h and 3-day periods after the FS arrivals.

## 2 Database and Methods

In this work, we used 64-s average solar wind plasma and magnetic field measurements by ACE for the period 1998–2018, obtained from the ACE Science Center (<http://www.srl.caltech.edu/ACE/ASC/level2/>). The interplanetary FSs are detected by “eye-inspection” of the time series data plots. The fast FSs are identified by simultaneous and sharp increases in plasma  $V_{sw}$ ,  $N_p$ ,  $T_p$ , and IMF  $B_0$ , in periods of about 1–3 min, on average, following previous works (e.g., [17–19, 38]). Further, shocks are considered only when all four of these measurements are available. A total of 297 FSs were identified during the entire period of this study.

The upstream and downstream solar wind regions of a shock are defined following previous works (e.g., [17–19, 38]), and the average  $N_p$  and  $B_0$  are determined for the regions. The regions have typical duration of 5 to 10 min, which can vary from shock to shock. The intervals are eye-inspected and selected to avoid contamination by waves, interplanetary discontinuities and high-frequency variations, besides data gaps, which could disturb the average quiet conditions necessary for the shock parameter computation. We

estimated the  $N_p$  compression ratio  $r_N = N_D/N_U$ , and the IMF  $B_0$  compression ratio  $r_B = B_D/B_U$ , where the subscripts U and D correspond to the upstream and downstream solar wind intervals, respectively.

To study the long-term variation of FSs, we take into account the ACE observation gaps. The gaps were noted especially for the plasma data, and in more recent years (SC24). Thus, to study the solar cycle variation of the FSs, we took the fraction of year with  $N_p$  data, calculated by the ratio of the number of data with  $N_p$  to the total data available. Next, the normalized FS rate, between 0 and 1, was computed for each year. The maximum number of FSs occurred in year 2000 and it was then normalized to 1. To study the solar cycle variation of FSs, the sunspot number (SSN) is used [41]. The yearly mean SSN version 2.0 data are obtained from the Royal Observatory of Belgium (<https://wwwbis.sidc.be/silso/home>). The classical cross-correlation coefficient [42] is calculated between the yearly mean SSN and the yearly normalized FS rate to determine their relationship and phase lag.

To determine the geomagnetic effects, the 1-h values of the ring current Dst index [43, 44], the auroral electrojet current index AE [44, 45] and the 3-h values of the global geomagnetic activity index ap [44] are analyzed [38, 39]. The geomagnetic indices were downloaded from NASA's OMNIweb database (<https://omniweb.gsfc.nasa.gov/>). The average peak values of the indices in an interval of 6 h following the FS arrival are determined as an estimate of the FS "geoeffectiveness". This interval is chosen because it is an empirical estimate of the sheath duration from the shock detection to its driver boundary [35, 46]. In addition, following previous works (see [37–39]) which have used 2 to 3 day intervals, a longer interval of 3 days is also used to study the geomagnetic variations after the FS arrival. While the short interval is useful to assess the direct shock and sheath effect, the longer interval exhibits the combined effects of the shock, sheath and their drivers (ICMEs or CIRs). The Dst, AE and ap geomagnetic activity levels are classified as defined in Echer et al. [39], with an addition of the superintense activity (see Table 1).

The form and character of a data distribution are studied with the statistical parameters of kurtosis and skewness [42]. Skewness is a measure of the deviation from symmetry of a distribution. A distribution is called symmetric if it looks the

same to the left and right of the central point. If the skewness is lower than  $-1$  or greater than  $+1$ , the distribution is considered to be highly skewed or asymmetric. If the skewness is between  $-1$  and  $-0.5$ , or between  $+0.5$  and  $+1$ , the distribution is moderately skewed. If the skewness is between  $-0.5$  and  $+0.5$ , the distribution is considered to be approximately symmetric. Kurtosis is a measure of the sharpness of a distribution. Gaussian distributions have kurtosis values close to 3, while sub-Gaussian ones have kurtosis lower than 3. Distributions with kurtosis values higher than 3 tend to have heavy tails or outliers [42].

Further, based on the form of the histograms of the average peak values of geomagnetic indices, fitted functions are selected to derive probability distribution functions and equations to assess the probability to observe a given level of geomagnetic activity in terms of AE, Dst and ap, in periods of 6 h and 3 days after the FS detection. The methodology to fit the probability functions follows the procedure conducted in the work by Alves et al. [40].

### 3 Results and Discussions

#### 3.1 Example of an Interplanetary FS and Associated Geomagnetic Activity

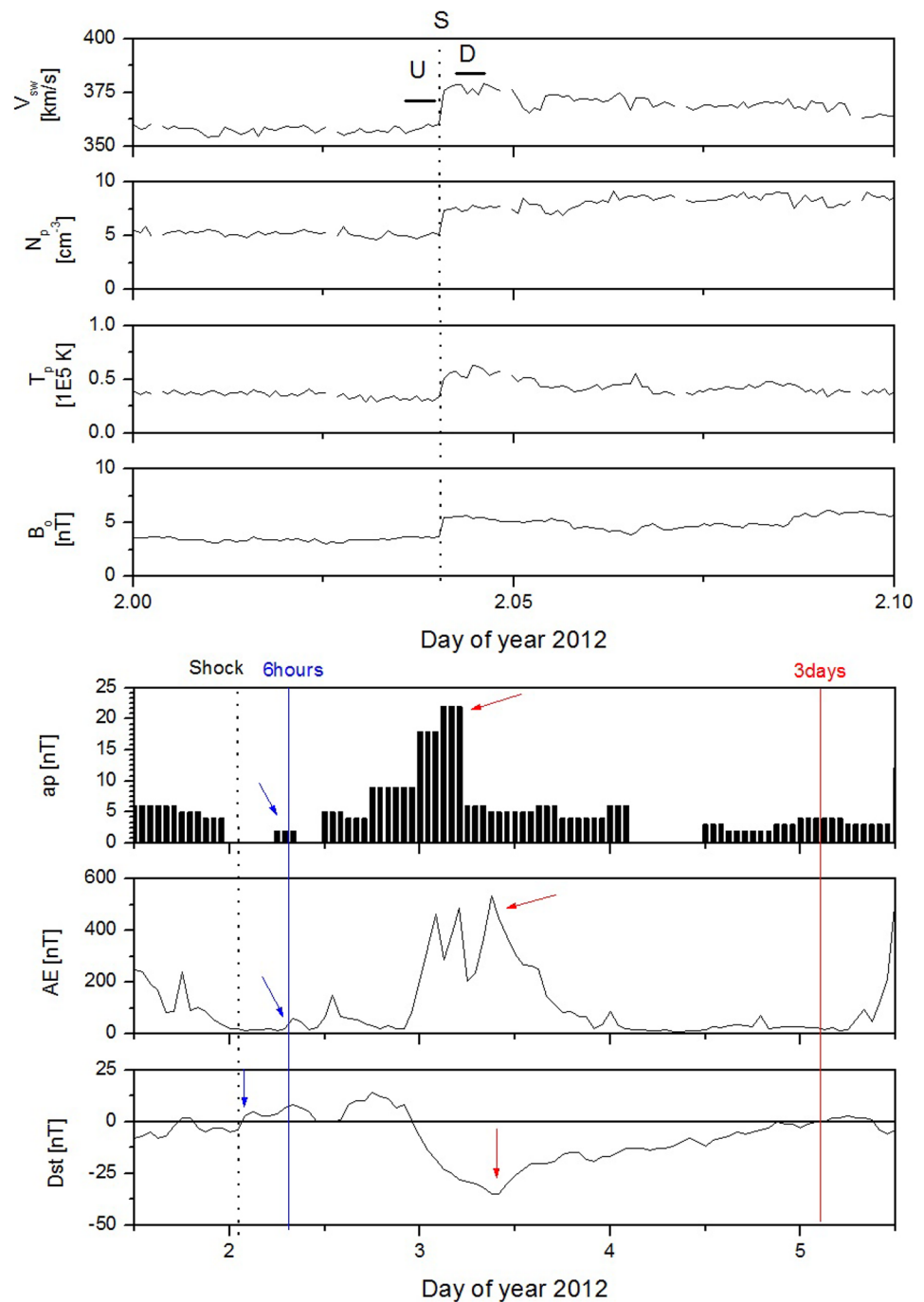
Figure 1 shows an example of an interplanetary fast FS and associated geomagnetic impacts. The FS was detected by the ACE spacecraft at  $\approx 0055$  UT on 2 January 2012 (marked by a vertical black dotted line). It can be identified from the sudden increases in the solar wind  $V_{sw}$  (from  $\approx 360$  to  $380$  km s $^{-1}$ ),  $N_p$  (from  $\approx 5.0$  to  $7.5$  cm $^{-3}$ ),  $T_p$  (from  $\approx 0.3 \times 10^5$  to  $0.6 \times 10^5$  K), and in IMF  $B_0$  (from  $\approx 3.6$  to  $5.5$  nT). The pre- and post-shock intervals from  $\approx 0046$  to  $\approx 0051$  UT, and from  $\approx 0100$  to  $\approx 0105$  UT are marked as the upstream (U) and downstream (D) solar wind intervals, respectively. The plasma and magnetic field compression ratios between the upstream and downstream solar wind intervals are:  $r_N = 1.5$  and  $r_B = 1.5$ , respectively. The values indicate a weak-to-moderate strength of the shock.

The bottom three panels of Fig. 1 show the geomagnetic ap, AE, and Dst indices. The FS arrival (at ACE) is marked by the vertical black dotted line (as above), the end of the 6-h interval following the shock arrival is marked by

**Table 1** Definition of geomagnetic activity levels used in this work according to ap, AE and Dst indices

	ap [nT]	AE [nT]	Dst [nT]
Geomagnetic Quiet	$ap < 32$	$AE < 200$	$Dst > -30$
Weak Storm	$32 \leq ap < 56$	$200 \leq AE < 500$	$-30 \geq Dst > -50$
Moderate Storm	$56 \leq ap < 111$	$500 \leq AE < 1000$	$-50 \geq Dst > -100$
Intense Storm	$111 \leq ap < 268$	$1000 \leq AE < 1800$	$-100 \geq Dst > -250$
Superintense Storm	$ap \geq 268$	$AE \geq 1800$	$Dst \leq -250$

**Fig. 1** Example of an interplanetary fast forward shock (FS) and associated geomagnetic activity. The top four panels show the solar wind speed  $V_{sw}$ , proton density  $N_p$ , temperature  $T_p$ , and interplanetary magnetic field (IMF) magnitude  $B_0$ , respectively, on 2 January 2012. Bottom three panels show the geomagnetic indices  $ap$ , AE and Dst, respectively, from 1 to 5 January. The FS arrival at  $\approx 0055$  UT on 2 January is marked by a dotted vertical line, and the upstream (U) and downstream (D) solar wind intervals are marked by horizontal bars at the top. In the bottom panels, the blue and red vertical solid lines indicate the ends of a 6-h and a 3-day intervals, respectively, following the FS arrival. The geomagnetic index peak values for the 6-h and 3-day intervals are marked by the blue and red arrows, respectively

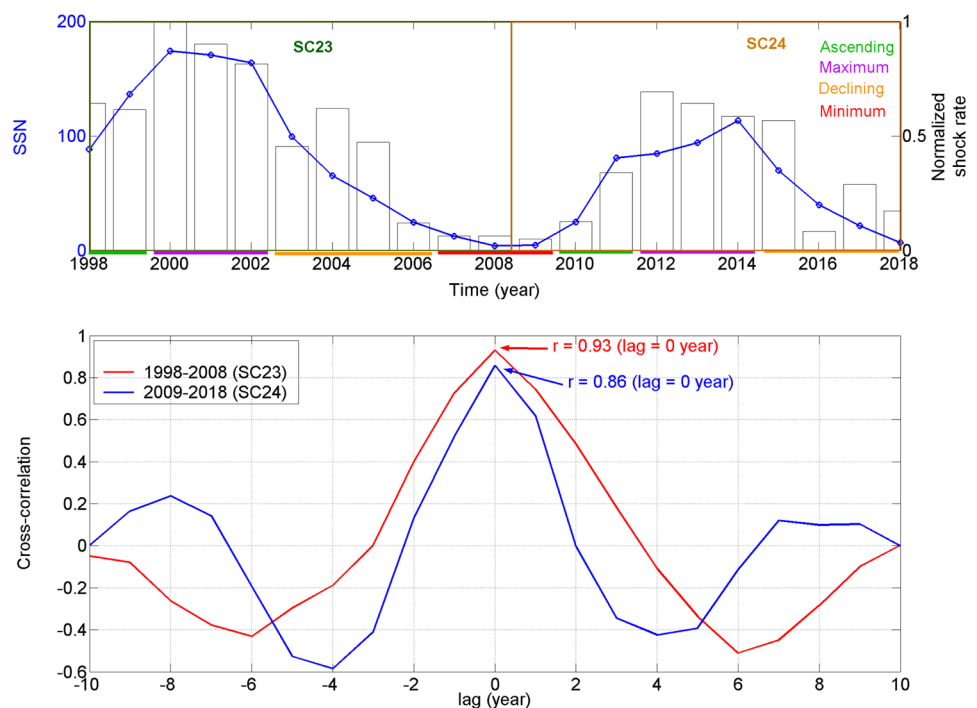


a vertical blue solid line, and the end of the 3-day interval is marked by a vertical red solid line. The peak values of geomagnetic indices during the 6-h and 3-day intervals are marked by the blue and red arrows, respectively. The values are as follows:  $ap = 2$  (22) nT,  $AE = 22$  (536) nT, and  $Dst = -4$  (-35) nT for the 6-h (3-day) interval. The Dst and  $ap$  values indicate a weak geomagnetic activity condition, while the AE value for the 3-day interval implies a moderate geomagnetic activity [47].

### 3.2 Solar Cycle Dependence of the FS Occurrence

Figure 2 (top panel) shows the normalized FS occurrence rate (barplots, scale on the right) for each year of observation. The yearly smoothed SSN (blue curve, scale on the left) is superposed in order to show the solar cycle phases. The normalized FS rate (to the year 2000 shock occurrence) follows the SSN variation. This is confirmed by the cross-correlation analysis between the normalized FS rate and

**Fig. 2** (Top panel) Normalized shock rate per year (empty vertical bars, scale on the right) and yearly average SSN (blue circles connected with lines, scale on the left). Solar cycle phases are marked by color bars in the bottom of the top panel: ascending (green), maximum (violet), declining (orange) and minimum (red) phases. (Bottom panel) Cross-correlation between the normalized shock rate and SSN for SC23 (red) and SC24 (blue)



SSN (Fig. 2, bottom panel). The highest cross-correlation coefficients for both SC23 ( $r = 0.93$ ) and SC24 ( $r = 0.86$ ) are recorded at a 0-year time lag between the two time series. While the higher correlation during SC23 than SC24 deserves further study, the high  $r$ -values at 0-year time lag between the FS occurrence and SSN are expected. Several past studies showed that most of the FSs are driven by ICMEs, and that the ICMEs are strongly correlated with the solar activity cycle [11]. Further, Kilpua et al. [13] found that the occurrence rate of the ICME-driven FSs near the Earth's orbit follows the SSN cycle, but the CIR-associated shocks do not show such variation. During the deep minimum phase between SC23 and SC24, the normalized shock occurrence rate was very low,  $\approx 0.05$ – $0.06$ . This is  $\approx 10$ – $20$  times less than the peak occurrences during SC24 and SC23, respectively. Echer et al. [17] have also found a large difference in the shock occurrences from 1995–1996 (solar minimum) to 2000 (maximum): 7.5 shocks per year at the solar minimum, and 50 shocks per year at the solar maximum.

As mentioned previously, the maximum normalized FS rate (1.0) is recorded during the year 2000, near the SC23 maximum. A clear difference can be noted in the FS occurrences between SC23 and SC24. SC24 has a broad maximum around 2012–2014 with a normalized FS occurrence rate of only 0.69 (during the year 2012). A comparison between the normalized FS occurrence rate for the different solar cycle phases of SC23 and SC24 shows that, as expected, the FS occurrence was higher in

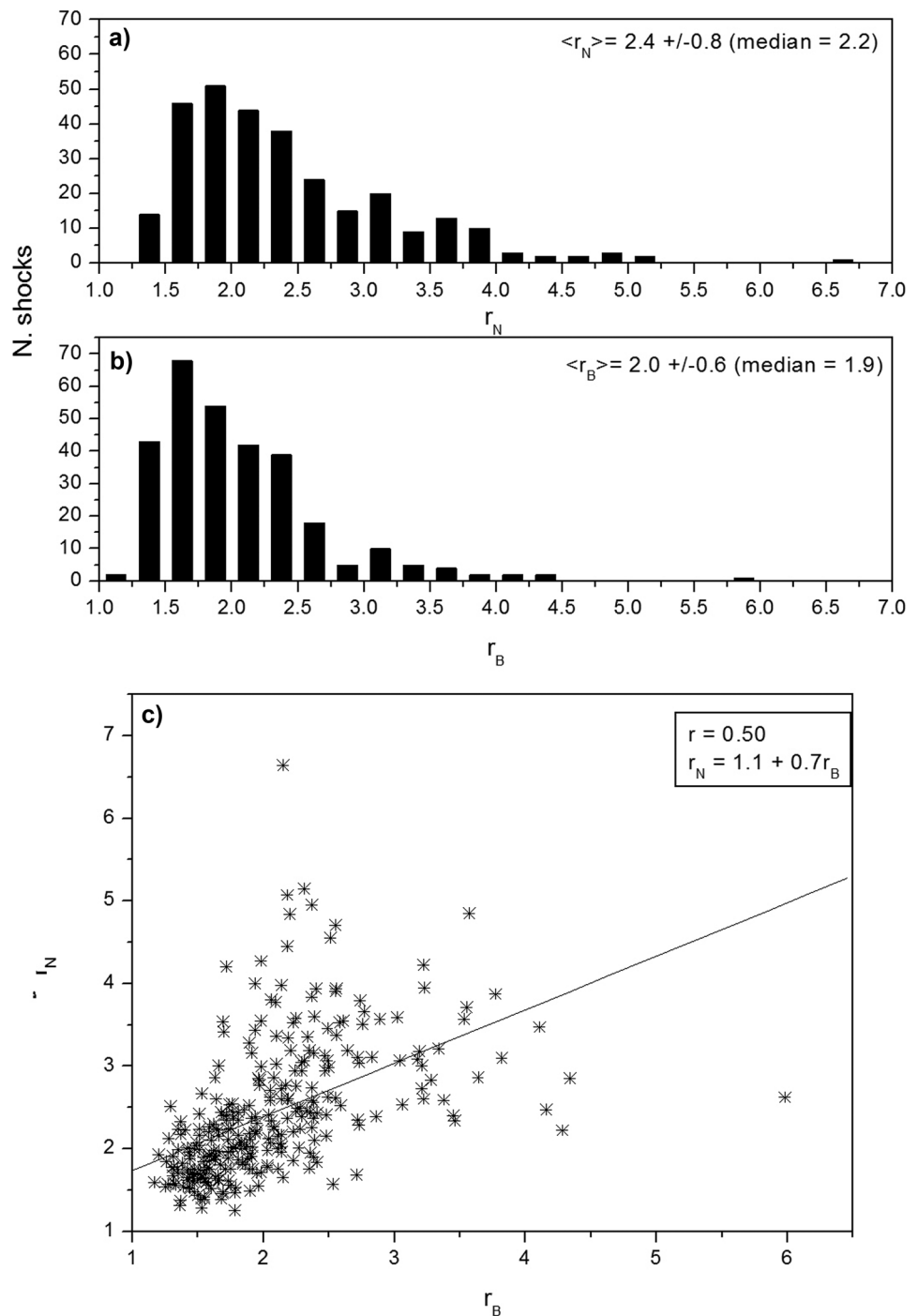
all phases for the SC23. The higher difference is observed in the ascending phase. During the ascending phase of SC23 (1998–1999) the normalized FS rate was 0.63, while for the same phase of SC24 (2010–2011), the rate was 0.23, with a difference of 63%. For the maximum phase, a reduction of almost 30% was observed, from 0.90 (SC23: 2000–2002) to 0.64 (SC24).

### 3.3 FS Compression Ratios

Figure 3 shows the distributions (histograms) of the compression ratios  $r_N$  and  $r_B$ , and their scatter plot with the regression line and correlation coefficients for all FSs under study. The distributions are found to exhibit the “skewed to the right” Gaussian profiles. The mean (median)  $r_N$  is 2.4 (2.2) (Fig. 3a), and the mean (median)  $r_B$  is 2.0 (1.9) (Fig. 3b).  $r_B$  has higher skewness (1.8) and kurtosis (8.6) values than  $r_N$  (1.4 and 5.5, respectively). The compression ratios have large dispersion with standard deviation values of 0.8 for  $r_N$  and 0.6 for  $r_B$ , which is about 1/3 of their average values. This reflects the natural variability of FS strength, with a few FSs being weak (with the compression ratio slight above 1), the bulk of distribution with compression ratio values between 1.5 and 3.0, and an extreme tail of the distribution with a few FSs having compression ratio values higher than 4.0. These results indicate that the majority of the FSs are weak to moderate in strength (compression ratio  $< 3.0$ ). Similar results were obtained for a smaller data set by Echer et al.



**Fig. 3** Histograms of **a** plasma density compression ratio  $r_N$  and **b** magnetic field compression ratio  $r_B$ . The statistical parameters of the distributions are also shown in the panels. The y-axes show the number of shocks. **c** Correlation between  $r_N$  and  $r_B$  for all the shocks. The linear regression line, equation and correlation coefficient are also shown



[17] who reported  $r_B \approx 2.0$  and  $r_N \approx 2.1$  (solar minimum) to  $\approx 2.6$  (solar maximum).

Figure 3c shows the linear regression analysis between  $r_N$  and  $r_B$  for all FSs. A large scatter can be noted in this figure, with a moderate correlation coefficient ( $r = 0.50$ ). Based on the statistical  $t$ -test, the correlation is found to be significant at the  $\approx 99\%$  confidence level.

### 3.4 Post-FS Solar Wind Conditions

The immediate post-shock solar wind is compressed and disturbed due to the shock passage. For periods longer than a few hours after the shock, the driver (ICME or CIR) fields dominate the solar wind conditions [46]. For this reason, it is of interest to compare solar wind conditions

and geomagnetic response during both short (6 h) and long (3 days) intervals after the FS arrival.

Figure 4 shows the histograms (percentage of FSs) of the peak values (for each interval) of solar wind parameters:  $V_{sw}$ , IMF  $B_z$ , and  $E_y$  during the 6-h and 3-day intervals following the FS impacts. The solar wind parameter distributions are found to be asymmetrical:  $V_{sw}$  and  $E_y$  are skewed to the right, and  $B_z$  is skewed to the left (negative values). For the 6-h (3-day) interval, the characteristic skewness and kurtosis are: 1.3 (0.98) and 4.7 (4.1) for  $V_{sw}$ ; -1.6 (-2.1) and 8.5 (9.7) for  $B_z$ ; and 2.5 (3.2) and 12.9 (17.3) for  $E_y$ , respectively. The  $V_{sw}$  skewness and kurtosis values are indicative of approximately symmetric or near-Gaussian distribution. However, the kurtosis values are  $> 3.0$  for all parameters, indicating strong non-Gaussian distributions with tails to the extreme values, especially for  $B_z$  and  $E_y$ .

During the 6-h interval (following the FS arrival), the average (median) of the solar wind interval peak values are: 525.5 (494.5)  $\text{km s}^{-1}$  for  $V_{sw}$ , -6.5 (-5.4) nT for  $B_z$ , and 3.5 (2.6)  $\text{mV m}^{-1}$  for  $E_y$ . On the other hand, for the 3-day interval, the values are: 609.9 (580.5)  $\text{km s}^{-1}$  for  $V_{sw}$ , -11.1 (-9.1) nT for  $B_z$ , and 6.1 (5.5)  $\text{mV m}^{-1}$  for  $E_y$ .

The post-FS average  $V_{sw}$  peak ( $\approx 610 \text{ km s}^{-1}$ ) for the 3-day distribution is significantly higher than the “normal solar wind” speed of  $\approx 300\text{--}400 \text{ km s}^{-1}$  (see [48, 49]). This high value may reflect the disturbed/shocked solar wind and contributions from the driving ICMEs or CIRs (when present). The tail of the  $V_{sw}$  distribution extends to a very

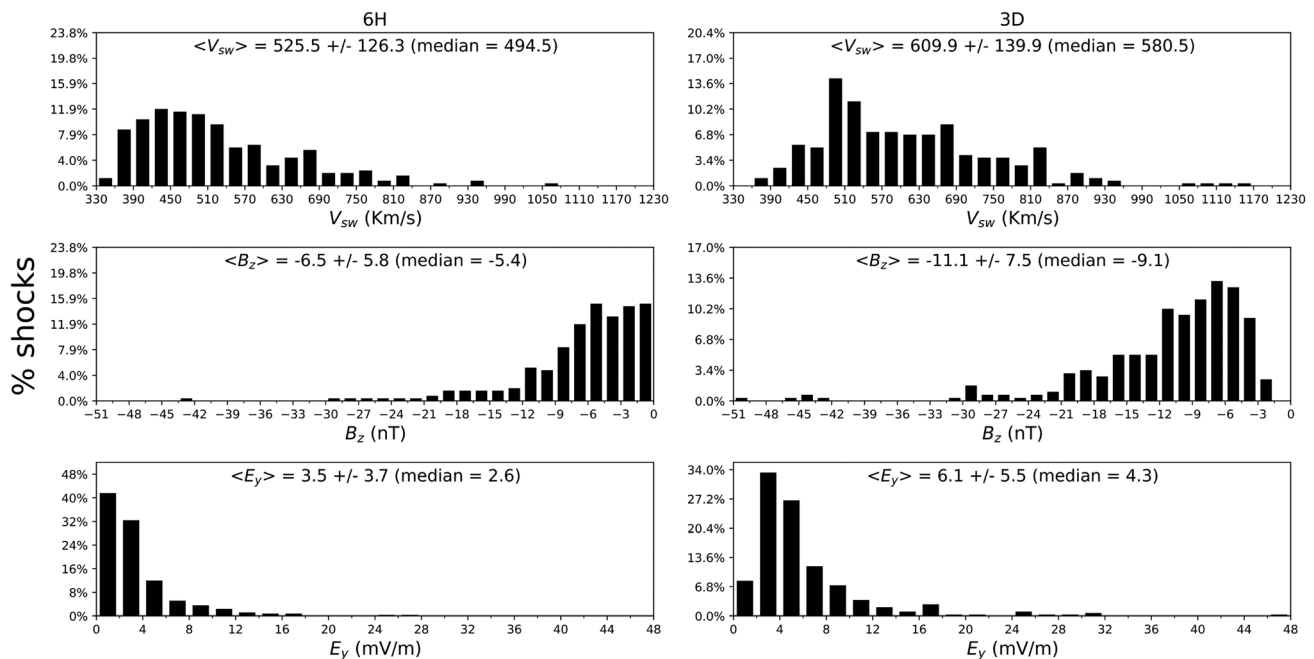
high value  $> 1000 \text{ km s}^{-1}$ , which could be associated with ICMEs [11].

The average peak  $B_z$  (-11 nT) and  $E_y$  ( $6.1 \text{ mV m}^{-1}$ ) values for the post-FS 3-day intervals are intense enough to cause moderate to intense geomagnetic storms [47, 50], and are higher than the values noted for the 6-h intervals. Most of the post-FS 6-h intervals are characterized by  $E_y < 4 \text{ mV m}^{-1}$  and  $B_z > -7 \text{ nT}$ , which reflect conditions that can lead to moderate or weak geomagnetic activity. There are a few events with very large values of  $B_z$  and  $E_y$ . The overall larger values in the 3-day intervals than in the 6-h intervals are possibly due to the inclusion of shock driver fields (ICMEs and CIRs) besides the shocked and sheath fields themselves [50].

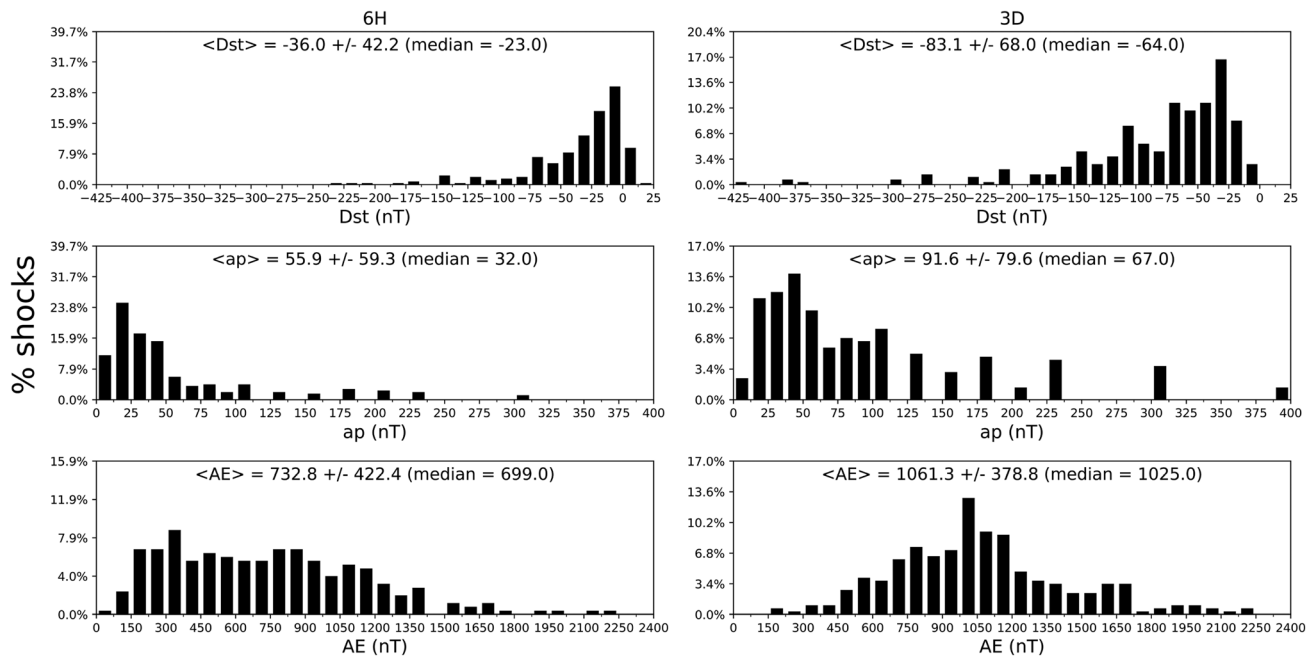
### 3.5 Post-FS Geomagnetic Conditions

Figure 5 shows the histograms (percentage of FSs) of the peak values of geomagnetic indices Dst, ap and AE during the 6-h and 3-day intervals following the FS arrival. The distributions are found to be asymmetrical in shape, skewed to the right for ap, near-symmetric for AE, and skewed to the left for Dst (negative values).

The FS compressions are known to lead to an enhancement of the Chapman-Ferraro (dayside) magnetopause current and a sudden increase (positive values) of the high resolution (1-min) magnetometer data and SYMH index. However, these effects are smoothed in the 1-h average Dst index variations, which are studied in this work.



**Fig. 4** Histograms of the peak solar wind  $V_{sw}$  ( $\text{km s}^{-1}$ ), IMF  $B_z$  (nT), and  $E_y$  ( $\text{mV m}^{-1}$ ) for the 6-h (left column) and 3-day (right column) intervals after the shock arrival. The y-axes show the percentage of shocks



**Fig. 5** Histograms of the peak geomagnetic indices Dst (nT), ap (nT) and AE (nT) for the 6-h (left column) and 3-day (right column) intervals after the shock arrival. The y-axes show the percentage of shocks

During the post-FS 6-h intervals, the average (median) of the peak values are:  $-36.0$  ( $-23.0$ ) nT for Dst,  $55.9$  ( $32.0$ ) nT for ap, and  $732.8$  ( $699$ ) nT for AE for all FSs (Fig. 5, left panels). These values indicate weak ring current (Dst) and the global (ap) geomagnetic activity, but moderate auroral (AE) activity immediately after the FS impact.

During the 3-day interval, the average (median) of the peak values of the indices are:  $-83.1$  ( $-64.0$ ) nT for Dst,  $91.6$  ( $67.0$ ) nT for ap, and  $1061.0$  ( $1025.0$ ) nT for AE for all FSs, indicating a moderate geomagnetic activity level (Fig. 5, right panels). The geomagnetic index values are substantially higher than those observed in the 6-h intervals. The sheath duration found by [46] at 1 AU is about 12 h, which could also contribute to the shocks geoeffectiveness in the 6-h intervals being lower than in the 3-day periods.

The geomagnetic index distributions are similar for the 6-h and 3-day intervals (Fig. 5). For the 6-h interval, the skewness (kurtosis) values are:  $-2.0$  ( $8.1$ ) for Dst,  $2.3$  ( $8.1$ ) for ap, and  $0.75$  ( $3.2$ ) for AE. The kurtosis (skewness) values for the 3-day interval are:  $8.2$  ( $-2.0$ ) for Dst,  $5.7$  ( $1.7$ ) for ap, and  $3.5$  ( $0.4$ ) for AE. The AE skewness and kurtosis values are indicative of near-Gaussian distributions.

From Fig. 5 (left panels) it can be noted that the ap index is more influenced by the ring current disturbances (measured by the Dst index). For the 6-h interval, the average ap peak for all FSs corresponds to a weak geomagnetic activity, similarly to Dst. However, for the 3-day period, both indices have average (median) peak values indicating moderate geomagnetic activity. This is different from the AE

distribution which shows more enhanced activity in both intervals. According to Saba et al. [51], there is a strong correlation between ap and Dst indices near the main phase of a geomagnetic storm, when the ring current is strong. On the other hand, for longer intervals, like one solar rotation or yearly averages, ap is more correlated to the AE index, which implies that the auroral activity has larger contribution to average long-term geomagnetic activity [38].

### 3.6 Correlation Analyses

Table 2 shows the correlation coefficients ( $r$ ) between the FS compression ratios,  $r_N$  and  $r_B$ , and the peak values of solar wind and geomagnetic activity parameters during the 6-h and 3-day intervals following the FS arrival. The  $r$  values are very low, indicating weak or no correlations

**Table 2** Correlation coefficients of the shock ratios  $r_N$  and  $r_B$  with the solar wind parameters and geomagnetic indices for the 6-h (3-day) intervals

Parameters	$r_N$	$r_B$
$V_{sw}$	0.1 (0.1)	0.4 (0.3)
$B_z$	$-0.1$ ( $-0.1$ )	$-0.3$ ( $-0.2$ )
$E_y$	0.1 (0.1)	0.4 (0.3)
ap	0.1 (0.1)	0.4 (0.3)
Dst	$-0.1$ ( $-0.1$ )	$-0.2$ ( $-0.3$ )
AE	0.1 (0.1)	0.3 (0.3)



**Table 3** Correlation coefficients between the peak solar wind parameters and the geomagnetic indices for the 6-h (3-day) intervals

Parameters	$V_{sw}$	$B_z$	$E_y$
ap	0.61 (0.60)	−0.76 (−0.76)	0.85 (0.79)
Dst	−0.46 (−0.42)	0.75 (0.88)	−0.79 (−0.82)
AE	0.51 (0.58)	−0.77 (−0.70)	0.77 (0.70)

between the parameters. There is no significant difference between the 6-h and the 3-day intervals. However, in general, the parameters exhibit comparatively higher correlations with  $r_B$  than with  $r_N$ . This is expected in case of  $B_z$  and  $E_y$  since they are related to IMF  $B_0$ .

The overall low correlations can be due to the fact that the shock compression ratios correspond to intervals very close to the shock (about 5 to 10 min), while the peak solar wind and geomagnetic parameters are computed for relatively longer intervals (6 h and 3 days). Thus, these parameters may have contributions from other sources, such as the sheath fields, and the driving ICME or CIR fields. The results clearly indicate lack of any relationship of the FS (compression) strength with the intensity of the southward IMF component.

The correlation coefficients between the average peak solar wind parameters and the geomagnetic indices for both 6-h and 3-day intervals are shown in Table 3. In general, the geomagnetic indices exhibit higher correlations with IMF  $B_z$  and  $E_y$ , than with  $V_{sw}$ . This is expected since geomagnetic activity is mainly controlled by the magnetic reconnection mechanism, for which the southward IMF  $B_z$  is the most important factor.

Correlations were also computed among the peak solar wind parameters (not shown). As expected, high correlation coefficients ( $r$ ) for the 6-h (3-day) interval are found between  $B_z$  and  $E_y$ ,  $r = -0.96$  (−0.92), and moderate to weak correlation between  $E_y$  and  $V_{sw}$ ,  $r = 0.41$  (0.49), and between  $B_z$  and  $V_{sw}$ ,  $r = -0.25$  (−0.29). Again there is not much difference from the 6-h to the 3-day interval for the  $r$ -values. The higher correlation found between  $E_y$  and  $V_{sw}$  than between  $B_z$  and  $V_{sw}$  can be expected since  $E_y$ , from its definition, depends on  $V_{sw}$ .

Further, we computed the correlations among the peak values of geomagnetic indices (not shown). The  $r$ -values for the 6-h (3-day) interval are as follows: −0.70 (−0.70) between Dst and AE; 0.76 (0.80) between AE and ap; and −0.80 (−0.80) between Dst and ap.

### 3.7 Statistical Analysis of the Post-FS Geomagnetic Activity

The geomagnetic activity is classified based on the average peak geomagnetic indices during the 6-h and 3-day intervals

following the shocks (see Table 1). The percentages of the FSs followed by geomagnetic activity of different levels are summarized in Table 4.

For the 6-h interval, the percentage of FSs followed by moderate, intense or superintense geomagnetic activity is 24.6% (Dst), 31.4% (ap) and 65.2% (AE). This result implies that the shocked solar wind is much more effective in causing auroral (AE) and global geomagnetic activity (ap) than in causing ring current (Dst) enhancement. This will be discussed below.

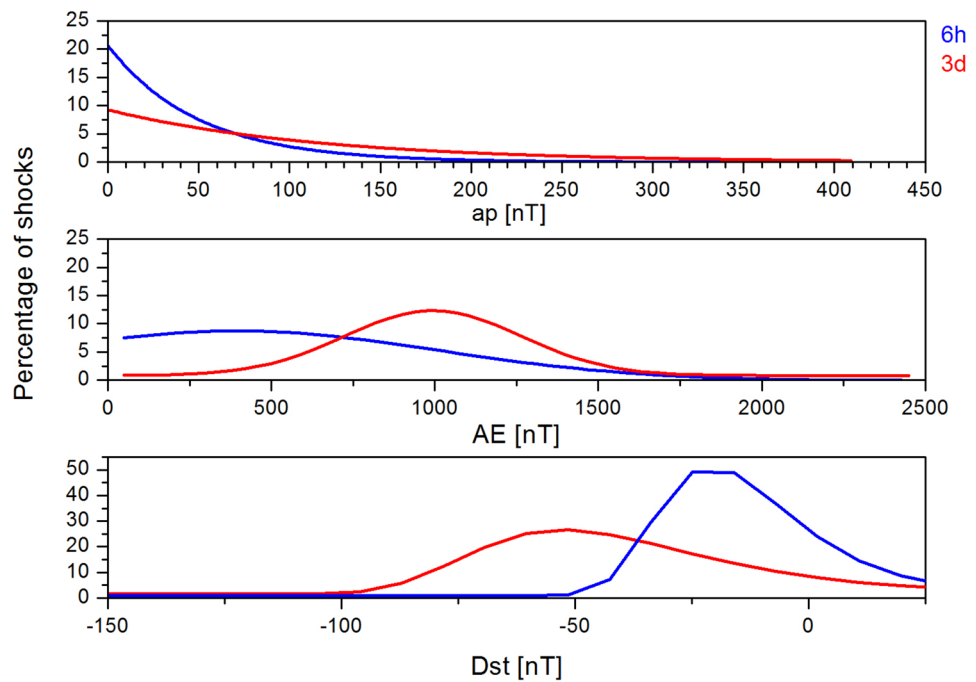
For the 3-day intervals,  $\approx 2/3$  of the FSs are followed by moderate or intense geomagnetic storms (in terms of the Dst index). The percentage of FSs followed by moderate to intense activity is 96% in terms of AE, and 60.5% in terms of ap. These results are similar to those obtained in previous works. Echer et al. [39] found that the percentage of FSs followed by moderate activity is of 55% for Dst, 48% for ap, and 83% for AE. In the present study, FSs and their post-shock intervals are found to have a slightly higher “geoeffectiveness”, which could be due to a different period of study and to the criterion of 3-day instead of 2-day time window used.

The results clearly show that FSs are followed by intervals of more enhanced auroral activity (AE) than the ring current (Dst) activity. For a geomagnetic storm to develop (or a ring current enhancement), a significantly strong and long-duration southward IMF component ( $B_s$ ) is required, which may not necessarily occur after the FSs. On the other hand, the magnetospheric compression (by the FSs) and particle precipitation in the auroral zone may lead to the AE intensification, even in the absence of a strong IMF  $B_s$  (but still with a significant energy preconditioning, see examples in [52, 53]). This is a scenario for substorms occurring outside a storm main phase. Interestingly, the ap level of magnetic activity following FSs is closer to Dst than to AE, indicating that at least for the shock disturbed periods, ap is more sensitive to the storm/ring current activity. These results are also coherent with previous works. It was found that shock and sheath impacts often can cause high-latitude activity, associated with strong auroral latitude events even if there is no significant storm development [54]. Further, it is known that there is also a strong response of auroral current regions to the fields of some sheath regions. Moreover, the majority of storms with the largest Kp values are related to sheaths. This is because the auroral currents

**Table 4** Geomagnetic activity levels considering the peak geomagnetic indices during the 6-h (3-day) intervals following the FS arrival

	ap	AE	Dst
Geomagnetic Quiet	44.4 (19.7)%	6.3 (0.3)%	57.5 (18.4)%
Weak Storm	24.2 (19.7)%	28.6 (3.7)%	17.9 (18.7)%
Moderate Storm	15.5 (28.9)%	39.3 (40.4)%	16.3 (31.6)%
Intense Storm	14.7 (26.5)%	24.2 (50.2)%	8.3 (27.9)%
Superintense Storm	1.2 (5.1)%	1.6 (5.4)%	0.0 (3.4)%

**Fig. 6** Fitted distribution functions for the 6-h (blue curves) and 3-day (red curves) peak values of the geomagnetic indices ap, AE and Dst. The equations are shown in the text, and the corresponding parameters are shown in Table 5. Note that while there are very few shocks with  $Dst < -150$  nT, the curves are only shown until this threshold for better visualization



have a major contribution to the Kp index [35]. This is also confirmed with the 6-h interval analysis which showed that soon after the FS arrival and in the sheath, AE is intensified for more than half of the FSs, while Dst reaches moderate or intense activity only for about 1 of 5 FSs.

### 3.8 Probability Distributions of the Post-FS Geomagnetic Activity

We derived the probability functions for the peak values of the post-FS geomagnetic indices shown in Fig. 5. These functions were obtained based on the shapes of the empirical distributions and on the previous work by Alves et al. [40].

Theoretical distribution functions were applied to estimate the probability of each of the peak geomagnetic index values to be reached after an interplanetary FS arrival. The distribution functions for the 6-h and 3-day intervals are shown in Fig. 6, and the obtained parameters are listed in Table 5.

The fitted distribution function for the Dst index is:

$$P_{Dst} = P_{Dst_0} + A_{Dst} \cdot \exp(-\exp(-z) - z + 1), \quad (1)$$

where  $z = \frac{x - x_{Dstc}}{w_{Dst}}$ , and  $x$  is the Dst geomagnetic index value,  $P_{Dst_0}$  is a constant,  $A_{Dst}$  is the amplitude,  $x_{Dstc}$  is the central position of Dst distribution, and  $w_{Dst}$  is the deviation of Dst for the fitted skewed Gaussian function.

For the AE index, the function is:

$$P_{AE} = P_{AE_0} + \frac{A_{AE}}{w_{AE}(\pi/2)^{1/2}} \cdot \exp\left(-2\left(\frac{x - x_{cAE}}{w_{AE}}\right)^2\right), \quad (2)$$

with  $x$  assuming the AE geomagnetic index value,  $P_{AE_0}$  is a constant,  $A_{AE}$  is the amplitude,  $x_{cAE}$  is the central position of AE distribution, and  $w_{AE}$  is the deviation of AE for the fitted Gaussian function.

For the ap index, the theoretical probability function is:

$$P_{ap} = P_{ap_0} + A_{ap} \cdot \exp(-ap/t_{ap}), \quad (3)$$

where  $A_{ap}$  is the amplitude,  $t_{ap}$  is a “time constant”, and  $P_{ap_0}$  is a constant of the ap fitted exponential function.

The ap index shows an exponential decay in its peak values, with a longer “time” constant for 3-days (116.3 nT) than for 6 h (49.7 nT) (Fig. 6, top panel). Thus, the ap distribution has higher values in the longer interval after the FSs. The decrease of the ap distribution is much faster for the 6-h interval than for the 3-day interval.

**Table 5** Parameters of the theoretical distribution functions fitted to the geomagnetic indices Dst, AE and ap. The equations are mentioned in the text, and the fitted distributions are shown in Fig. 6

	6-h	3-d
$P_{Dst_0}$	1.10	1.63
$A_{Dst}$	50.28	24.95
$x_{Dstc}$	20.7	52.6
$w_{Dst}$	14.3	24.98
$P_{AE_0}$	-0.086	0.85
$A_{AE}$	13742.8	7776.7
$w_{AE}$	1242.4	538.24
$x_{cAE}$	392.3	994.2
$A_{ap}$	20.6	9.26
$t_{ap}$	49.7	116.35
$P_{ap_0}$	0	0

The AE distribution was fitted to a Gaussian function (Fig. 6, middle panel). It can be seen that the 3-day AE distribution is shifted to much higher AE values with its peak around 1000 nT compared to a peak around 500 nT for the 6-h interval. The central position parameter of these distributions ( $x_c$ ) is much higher (994.2 nT) for the 3-day interval than for the 6-h interval (392.3 nT).

The Dst index was fitted to an “extreme to the left” Gaussian function (Fig. 6, bottom panel). The peak values of the 3-day interval are more displaced to the left (more negative Dst values) than that of the 6-h interval. The tail of the Dst distribution goes to higher values for the 3-day interval than for the 6-h interval.

The probability distribution functions derived above could be useful for space weather modeling or to predict the probability of an FS to be followed by a geomagnetic activity of a given strength. One operational way to perform this task is to compute the probable level of geomagnetic activity after an FS is detected or to use tables to assess it. A future study can be done to verify if the distribution parameters change with the shock parameters, namely, the shock strength and normal angles. Another advancement could be to compute the conditional probability to obtain a given geomagnetic activity level if one has a shock and a given  $B_s$  value. This could be computed for several values of  $B_s$  and other solar wind parameters.

## 4 Summary and Conclusions

We have explored the ACE 64-s averaged solar wind plasma and IMF measurements to identify and study the interplanetary fast FSs upstream of the Earth. From 1998 through 2018, 297 FSs were identified. The FS parameters and the geomagnetic activity following their arrival were investigated in this work. The main results can be summarized as follows.

The (normalized) shock occurrence rate followed the solar activity (sunspot) cycle, with a higher correlation coefficient during SC23 ( $r = 0.93$ ) than during SC24 ( $r = 0.86$ ). There were relatively less FSs in SC24 than in SC23. This is expected and is coherent with the solar cycle variation of the known main FS driver (ICMEs), and with the differences between the two cycles.

The average shock plasma and magnetic field compression ratios were  $\approx 2.4$  and 2.0, respectively, for all FSs under this study. Correlation between the two compression ratios was found to be moderate (correlation coefficient  $r = 0.50$ ). Their distributions were highly skewed and had high kurtosis values ( $> 3$ ). Solar wind parameters and geomagnetic indices during the 6-h and 3-day intervals following the FS

arrivals had high values of skewness and kurtosis as well, indicating asymmetric distributions.

The solar wind parameters and geomagnetic activity indices were higher for the post-FS 3-day interval than for the 6-h interval. Average values of the peak solar wind parameters for the 6-h (3-day) interval were:  $V_{sw} = 525$  (610) km s<sup>-1</sup>, IMF  $B_z = -6.5$  (-11) nT, and  $E_y = 3.5$  (6) mV m<sup>-1</sup>. The consequent geomagnetic index average peaks during the 6-h (3-day) interval were: Dst = -36 (-83) nT, ap = 56 (92) nT, and AE = 733 (1061) nT.

Correlations of the solar wind and geomagnetic activity parameters with the FS compression ratios were very weak or insignificant, indicating no clear relationships of the FS strength with the following interplanetary conditions and geomagnetic activity. However, the solar wind parameters and the geomagnetic indices were strongly correlated among themselves.

About 1 in 4 (25%) FSs were found to be followed by geomagnetic storms with Dst  $\leq -50$  nT (moderate to super-intense) in the 6-h interval following their arrival. However, this percentage increased to 66% of FSs in the 3-day intervals following the shock impact. The latter result is interpreted as a combined effects of shocks, sheaths and shock driver (ICME or CIR) IMF  $B_s$  fields.

Moderate to intense AE activity was recorded during the 6-h interval following a larger number of FSs (65.1%), and during the 3-day interval following almost all FSs ( $\approx 96\%$ ). This indicates a statistically higher effect of the post-FS solar wind on the auroral activity than on the ring current activity.

Fitted probability functions for the post-FS peak values of the geomagnetic indices were derived based on the shape of the observed distributions. An exponential decay function was derived for the ap index. A simple Gaussian function was fitted to the AE index, and for the Dst index, a skewed Gaussian function was obtained. The derived equations and associated distribution parameters may be useful for the space weather modeling.

The results obtained in this work confirm previous studies using different interplanetary shock databases [39, 40]. From the space weather point of view, it is concluded that the observation of an FS upstream of the Earth implies a geomagnetic storm (moderate or intense) occurrence probability of 1/4 in the following 6 h, and 2/3 in the following 3 days. Moreover, it leads to enhanced auroral activity in about 2/3 of the FSs for the 6-h interval and for almost all FSs in the 3-day period.

We encourage the space researchers to use this shock database to study other magnetospheric and ionospheric effects, such as energetic electron and ion fluxes, magnetotail plasma sheet field and plasma, and low-to-high latitude ionospheric effects.

**Acknowledgements** E. E. would like to thank Brazilian agencies for research grants: CNPq (contract no. PQ-302583/2015-7, PQ-301883/2019-0) and FAPESP (2018/21657-1). A. L. and L. E. S. N. would like to thank the PIBIFSP Program for the fellowship received during 2019 and 2020 as well as CAPES – Brazilian Federal Agency - and CAP/INPE Pos Graduation Program for the Master's fellowship. The work of R. H. is funded by the Science and Engineering Research Board (SERB, grant no. SB/S2/RJN-080/2018), a statutory body of the Department of Science and Technology (DST), Government of India through the Ramanujan fellowship. The work of A. M. S. F. is funded by the Brazilian CNPq agency (project no. PQ-300969/2020-1, PQ-301542/2021-0). The work of M. J. A. B. was supported by CNPq agency (contract no. PQ-302330/2015-1, PQ-305692/2018-6) and FAPESP agency (contract no. 2012.1026.7000905). We thank the Brazilian Ministry of Science, Technology and Innovation and the Brazilian Space Agency as well. The solar wind plasma and IMF data used in this work are obtained from the ACE Science Center (<http://www.srl.caltech.edu/ACE/ASC/level2/>). The geomagnetic indices are collected from the OMNIweb database (<https://omniweb.gsfc.nasa.gov/>). The SSN data are obtained from the Royal Observatory of Belgium (<https://wwwbis.sidc.be/silso/home>).

**Funding** A. M. S. F. was funded by FAPESP (projects 2016/10794-2 and 2017/00516-8) and CNPq agency (projects PQ-300969/2020-1, PQ-301542/2021-0). E. E. received grants from FAPESP (2018/21657-1) and CNPq (PQ-301883/2019-0) agencies. M. J. A. B. was supported by CNPq agency contract number (PQ-305692/2018-6) and FAPESP agency contract number 2012.1026.7000905. R. H. received support from the Science and Engineering Research Board grant SB/S2/RJN-080/2018.

**Data Availability** The solar wind plasma and IMF data used in this work are obtained from the ACE Science Center (<http://www.srl.caltech.edu/ACE/ASC/level2/>). The geomagnetic indices are collected from the OMNIweb database (<https://omniweb.gsfc.nasa.gov/>). The SSN data are obtained from the Royal Observatory of Belgium (<https://wwwbis.sidc.be/silso/home>).

## Declarations

**Ethics Approval** The work followed better human and scientific practices.

**Consent to Participate** All participants consent to the work.

**Consent for Publication** All participants consent for publication.

**Conflict of Interest** The authors declare no competing interests.

## References

1. E.N. Parker, Dynamics of the interplanetary gas and magnetic fields. *Astrophys. J.* **128**, 664–676 (1958). <https://doi.org/10.1086/146579>
2. D.F. Webb, T.A. Howard, Coronal mass ejections: Observations. *Liv. Rev. Solar Phys.* **9**, 1–83 (2012). <https://doi.org/10.12942/lrsp-2012-3>
3. A. Balogh, V. Bothmer, N.U. Crooker, R.J. Forsyth, G. Gloeckler, A. Hewish, M. Hilchenbach, R. Kallenbach, B. Klecker, J.A. Linker, E. Lucek, G. Mann, E. Marsch, A. Posner, I.G. Richardson, J.M. Schmidt, M. Scholer, Y.M. Wang, R.F. Wimmer-Schweingruber, M.R. Aellig, P. Bochsler, S. Hefti, Z. Mikii, The solar origin of corotating interaction regions and their formation in the inner heliosphere. *Space Sci. Rev.* **89**, 141–178 (1999). <https://doi.org/10.1023/A:1005245306874>
4. A.J. Hundhausen, *Coronal Expansion and Solar Wind* (Springer-Verlag, Berlin (1972). <https://doi.org/10.1007/978-3-642-65414-5>
5. E.J. Smith, J.H. Wolfe, Observations of interaction regions and corotating shocks between one and five AU: Pioneers 10 and 11. *Geophys. Res. Lett.* **3**, 137–140 (1976). <https://doi.org/10.1029/GL003i003p00137>
6. L.F. Burlaga, *Interplanetary magnetohydrodynamics*, vol. 3 (Oxford University Press) 272 (1995)
7. D. Burgess, in *Introduction to Space Plasma Physics*, ed. by M.G. Kivelson, C.T. Russell (Cambridge University Press, Cambridge - UK) Chapter 5 (1995)
8. A.J. Hundhausen, *The Solar Wind* (Cambridge University Press, Cambridge, 1995), pp.91–128
9. B. Heber, T. Sanderson, M. Zhang, Corotating interaction regions. *Adv. Space Res.* **23**, 567–579 (1999). [https://doi.org/10.1016/S0273-1177\(99\)80013-1](https://doi.org/10.1016/S0273-1177(99)80013-1)
10. L. Jian, C.T. Russell, J.G. Luhmann, R.M. Skoug, Properties of stream interactions at one AU during 1995–2004. *Sol. Phys.* **239**, 337–392 (2006). <https://doi.org/10.1007/s11207-006-0132-3>
11. R. Schwenn, Space weather: The solar perspective. *Liv. Rev. Sol. Phys.* **3**, 1–72 (2006). <https://doi.org/10.1007/s41116-021-00030-3>
12. B.T. Tsurutani, G.S. Lakhina, O.P. Verkhoglyadova, W.D. Gonzalez, E. Echer, F.L. Guarnieri, A review of interplanetary discontinuities and their geomagnetic effects. *J. Atmos. Sol. Terr. Phys.* **73**, 5–19 (2011a). <https://doi.org/10.1016/j.jastp.2010.04.001>
13. E.K.J. Kilpua, E. Lumme, K. Andreeva, A. Isavnin, H.E.J. Koskinen, Properties and drivers of fast interplanetary shocks near the orbit of the Earth (1995–2013). *J. Geophys. Res.* **120**, 4112–4125 (2015). <https://doi.org/10.1002/2015JA021138>
14. I.G. Richardson, Solar wind stream interaction regions throughout the heliosphere. *Liv. Rev. Sol. Phys.* **15**, 1–95 (2018). <https://doi.org/10.1007/s41116-017-0011-z>
15. E. Echer, M.J.A. Bolzan, A.M.S. Franco, Statistical analysis of solar wind parameter variation with heliospheric distance: Ulysses observations in the ecliptic plane. *Adv. Space Res.* **65**, 2846–2856 (2020). <https://doi.org/10.1016/j.asr.2020.03.036>
16. R. Hajra, J.V. Sunny, Corotating interaction regions during solar cycle 24: A study on characteristics and geoeffectiveness. *Sol. Phys.* **297**, 30 (2022). <https://doi.org/10.1007/s11207-022-01962-1>
17. E. Echer, W.D. Gonzalez, L.E.A. Vieira, A. Dal Lago, F.L. Guarnieri, A. Prestes, A.L.C. Gonzalez, N.J. Schuch, Interplanetary shock parameterse during solar activity maximum 2000 and minimum 1995–1996. *Brazilian J. Phys.* **33**, 115–122 (2003). <https://doi.org/10.1590/S0103-97332003000100010>
18. E. Echer, Interplanetary shock parameters near Jupiter's orbit. *Geophys. Res. Lett.* **46**, 5681–5688 (2019). <https://doi.org/10.1029/2019GL082126>
19. E. Echer, Solar wind and interplanetary shock parameters near Saturn's orbit (~10 au). *Planet. Space Sci.* **165**, 210–220 (2019). <https://doi.org/10.1016/j.pss.2018.10.006>
20. R. Hajra, Variation of the interplanetary shocks in the inner heliosphere. *Astrophys. J.* **917**, 91 (2021). <https://doi.org/10.3847/1538-4357/ac0897>
21. H.V. Cane, The evolution of interplanetary shocks. *J. Geophys. Res.* **90**, 191–197 (1985). <https://doi.org/10.1029/JA090iA01p00191>
22. N.R. Sheeley, R.A. Howard, M.J. Koomen, D.J. Michels, R. Schwenn, K.H. Muser, H. Rosenbauer, Coronal mass ejections and interplanetary shocks. *J. Geophys. Res.* **90**, 163–175 (1985). <https://doi.org/10.1029/JA090iA01p00163>
23. E. Echer, W.D. Gonzalez, B.T. Tsurutani, L.E.A. Vieira, M.V. Alves, A.L.C. Gonzalez, On the preferential occurrence of interplanetary shocks in July and November: Causes (solar wind annual dependence) and consequences (intense magnetic storms).



- J. Geophys. Res. **110**, A02,101 (2005a). <https://doi.org/10.1029/2004JA010527>
24. T. Gold, in *Gas Dynamics of Cosmic Clouds*. **2**, 97 (1955)
25. J.C. Foster, J.R. Wygant, M.K. Hudson, A.J. Boyd, B.D. N., P.J. Erickson, H.E. Spence, Shock-induced prompt relativistic electron acceleration in the inner magnetosphere. *J. Geophys. Res.* **120**(3), 1661–1674 (2015). <https://doi.org/10.1002/2014JA020642>
26. S.G. Kanekal, D.N. Baker, J.F. Fennell, A. Jones, Q. Schiller, I.G. Richardson, X. Li, D.L. Turner, S. Califf, S.G. Claudepierre, L.B. Wilson III, A. Jaynes, J.B. Blake, G.D. Reeves, H.E. Spence, C.A. Kletzing, J.R. Wygant, Prompt acceleration of magnetospheric electrons to ultrarelativistic energies by the 17 March 2015 interplanetary shock. *J. Geophys. Res.* **121**, 7622–7635 (2016). <https://doi.org/10.1002/2016JA022596>
27. R. Hajra, B.T. Tsurutani, in *Extreme Events in Geospace: Origins, Predictability, and Consequences*, ed. by N. Buzulukova (Elsevier), pp. 373–400 (2018a). <https://doi.org/10.1016/B978-0-12-812700-1.00014-5>
28. D.M. Oliveira, A.A. Samsonov, Geoeffectiveness of interplanetary shocks controlled by impact angles: A review. *Adv. Space Res.* **61**, 1–44 (2018). <https://doi.org/10.1016/j.asr.2017.10.006>
29. E. Echer, B.T. Tsurutani, W.D. Gonzalez, Interplanetary fast forward shocks and their geomagnetic effects: Cawses events. *J. Atmos. Sol. Terr. Phys.* **73**, 1330–1338 (2011). <https://doi.org/10.1016/j.jastp.2010.09.020>
30. B.T. Tsurutani, E. Echer, W.D. Gonzalez, The solar and interplanetary causes of the recent minimum in geomagnetic activity (MGA23): A combination of mid latitude small coronal holes, low IMF Bz variances, low solar wind speeds and low solar magnetic fields. *Ann. Geophys.* **29**, 839–849 (2011). <https://doi.org/10.5194/angeo-29-839-2011>
31. B.T. Tsurutani, R. Hajra, The interplanetary and magnetospheric causes of geomagnetically induced currents (GICs) > 10 A in the Mäntsälä Finland pipeline: 1999 through 2019. *J. Space Weather Space Clim.* **11**, 23 (2021). <https://doi.org/10.1051/swsc/2021001>
32. B.T. Tsurutani, W.D. Gonzalez, F. Tang, S.I. Akasofu, E.J. Smith, Origin of interplanetary southward magnetic fields responsible for major magnetic storms near solar maximum (1978–1979). *J. Geophys. Res.* **93**, 8519–8531 (1988). <https://doi.org/10.1029/JA093iA08p08519>
33. D.J. McComas, J.T. Gosling, S.J. Bame, E.J. Smith, H.V. Cane, A test of magnetic field draping induced Bz perturbations ahead of fast coronal mass ejecta. *J. Geophys. Res.* **94**, 1465–1471 (1989). <https://doi.org/10.1029/JA094iA02p01465>
34. W.D. Gonzalez, B.T. Tsurutani, A.L. Clua de Gonzalez, Interplanetary origin of geomagnetic storms. *Space Sci. Rev.* **88**, 529–562 (1999). <https://doi.org/10.1023/A:1005160129098>
35. E. Kilpua, H.E.J. Koskinen, T.I. Pulkkinen, Coronal mass ejections and their sheath regions in interplanetary space. *Liv. Rev. Sol. Phys.* **14**, 1–83 (2017). <https://doi.org/10.1007/s41116-017-0009-6>
36. W.D. Gonzalez, E. Echer, B.T. Tsurutani, A.L. Gonzalez, A. Lago, Interplanetary origin of intense, superintense and extreme geomagnetic storms. *Space Sci. Rev.* **158**, 69–89 (2011). <https://doi.org/10.1007/s11214-010-9715-2>
37. E. Echer, W.D. Gonzalez, Geoeffectiveness of interplanetary shocks, magnetic clouds, sector boundary crossings and their combined occurrence. *Geophys. Res. Lett.* **31**, 1–4 (2004). <https://doi.org/10.1029/2003GL019199>
38. E. Echer, M.V. Alves, W.D. Gonzalez, Geoeffectiveness of interplanetary shocks during solar minimum (1995–1996) and solar maximum (2000). *Sol. Phys.* **221**, 361–280 (2004). <https://doi.org/10.1016/j.pss.2018.10.006>
39. E. Echer, W.D. Gonzalez, M.V. Alves, On the geomagnetic effects of solar wind interplanetary magnetic structures. *Space Weather* **4**, 1–16 (2006). <https://doi.org/10.1029/2005SW000200>
40. M.V. Alves, E. Echer, W.D. Gonzalez, Geoeffectiveness of solar wind interplanetary magnetic structures. *J. Atmos. Sol. Terr. Phys.* **73**(73), 1380–1384 (2011). <https://doi.org/10.1016/j.jastp.2010.07.024>
41. F. Clette, F. Lefevre, The new sunspot number: assembling all corrections. *Sol. Phys.* **291**, 2629–2651 (2016). <https://doi.org/10.1007/s11207-016-1014-y>
42. J.C. Davis, *Statistics and Data Analysis in Geology* (Wiley, 2002)
43. M. Sugiura, Hourly values of equatorial Dst for the IGY. *Ann. Intern. Geophys. Year* **35**, 9 (1964)
44. G. Rostoker, Geomagnetic indices. *Rev. Geophys.* **10**, 935–950 (1972). <https://doi.org/10.1029/RG010i004p00935>
45. T.N. Davis, M. Sugiura, Auroral electrojet activity index AE and its universal time variations. *J. Geophys. Res.* **71**, 785–801 (1966). <https://doi.org/10.1029/JZ071i003p00785>
46. M. Janvier, R.M. Winslow, S. Good, E. Bonhomme, P. Démoulin, S. Dasso, C. Mestl, N. Lugaz, T. Amerstorfer, E. Soubrié, P.D. Boakes, Generic magnetic field intensity profiles of interplanetary coronal mass ejections at Mercury, Venus, and Earth from superposed epoch analyses. *J. Geophys. Res.* **124**, 812–836 (2019). <https://doi.org/10.1029/2018JA025949>
47. W.D. Gonzalez, J.A. Joselyn, Y. Kamide, H.W. Kroehl, G. Rostoker, B.T. Tsurutani, V.M. Vasyliunas, What is a geomagnetic storm? *J. Geophys. Res.* **99**, 5771–5792 (1994). <https://doi.org/10.1029/93JA02867>
48. B.T. Tsurutani, G.S. Lakhina, E. Echer, R. Hajra, C. Nayak, A.J. Mannucci, X. Meng, Comment on “Modeling extreme “Carrington-type” space weather events using three-dimensional global MHD simulations by C. M. Ngwira, A. Pulkkinen, M. M. Kuznetsova, and A. Gloer”. *J. Geophys. Res.* **123**, 1388–1392 (2018). <https://doi.org/10.1002/2017JA024779>
49. R. Hajra, B.T. Tsurutani, Near-Earth sub-Alfvénic solar winds: Interplanetary origins and geomagnetic impacts. *Astrophys. J.* **926**, 135 (2022). <https://doi.org/10.3847/1538-4357/ac4471>
50. E. Echer, W.D. Gonzalez, B.T. Tsurutani, A.L.C. Gonzalez, Interplanetary conditions causing intense geomagnetic storms (Dst < -100 nT) during solar cycle 23 (1996–2006). *J. Geophys. Res.* **113**, 1–20 (2008). <https://doi.org/10.1029/2007JA012744>
51. M.M.F. Saba, W.D. Gonzalez, A.L. Clúa de Gonzalez, Relationships between the AE, ap and Dst indices near solar minimum (1974) and at solar maximum (1979). *Ann. Geophys.* **15**, 1265–1270 (1997). <https://doi.org/10.1007/s00585-997-1265-x>
52. R. Hajra, B.T. Tsurutani, Interplanetary shocks inducing magnetospheric supersubstorms (SML < -2500 nT): Unusual auroral morphologies and energy flow. *Astrophys. J.* **858**, 123 (2018). <https://doi.org/10.3847/1538-4357/aabae4>
53. B.T. Tsurutani, R. Hajra, Energetics of shock triggered supersubstorms (SML < -2500 nT). *Astrophys. J.* **946**, 17, (2023). <https://doi.org/10.3847/1538-4357/acb143>
54. K.E.J. Huttunen, J.E.J. Koskinen, Importance of post-shock streams and sheath regions as drivers of intense magnetospheric storms and high latitude activity. *Ann. Geophys.* **22**, 1729–1738 (2004). <https://doi.org/10.5194/angeo-22-1729-2004>

**Publisher's Note** Springer Nature remains neutral with regard to jurisdictional claims in published maps and institutional affiliations.

Springer Nature or its licensor (e.g. a society or other partner) holds exclusive rights to this article under a publishing agreement with the author(s) or other rightsholder(s); author self-archiving of the accepted manuscript version of this article is solely governed by the terms of such publishing agreement and applicable law.